JOURNAL OF PROPULSION AND POWER
Vol. 26, No. 6, November–December 2010

Numerical Investigation of Transverse Jets Through Multiport Injector Arrays in Supersonic Crossflow

Adrian S. Pudsey* and Russell R. Boyce†
University of Queensland, Brisbane 4072, Australia

DOI: 10.2514/1.39603

A three-dimensional numerical study has been performed of the effects of sonic gaseous hydrogen injection through multiple transverse injectors subjected to a supersonic crossflow. Solutions were obtained for a series of injection configurations in a Mach 4.0 crossflow, with a global equivalence ratio of $\phi = 0.5$. Results indicate a different flow structure than for a typical single jet, with the development of two clearly defined wake vortices, including a stagnation point and reversed flow region immediately behind each downstream jet. While the overall penetration was reduced under the investigated conditions, significant improvements were observed when nondimensionalizing against the equivalent jet diameter for each modeled injector row. This was found to be the result of increased jet-to-freestream momentum ratio due to the subsonic flow regions between each injector. Further enhancements were also observed in terms of mixing performance for the multijet cases. Improvements of up to 5% in the overall mixing efficiency were experienced by using multiple jets due to increased mixant interface area and intermediate stirring through wake vortices between each injector. No improvement in far-field mixing was observed. Overall, it has been demonstrated that there are benefits to be gained through the injection of gaseous hydrogen from many small injectors rather than fewer large injectors.

I. Introduction

IN THE realm of high-speed flight, hypersonic air breathing propulsion is not a new subject, however, renewed interest in this field has resulted in increased scramjet research in recent years. One of the primary challenges is successful fuel injection into the supersonic crossflow within the scramjet combustor. Because of the inherently short residence time of gases in a supersonic combustor, good fuel injectant penetration and mixing is essential to achieve rapid and most importantly efficient combustion. This is due to the finite rate reactions that take place as the fuel burns within the combustion chamber during its passage through the engine.

Over the years many types of injectors have been proposed including in-stream, hypermixers and wall porthole injectors, each with their respective advantages and disadvantages. The work reported here investigates porthole injectors. The porthole injector has no physical obstruction to the combustor flow, with a typical reduction in drag and cooling requirements compared with other methods. However, while porthole jets offer minimal intrusion into the combustor flow path, they cause a complex flow structure in the vicinity of the jet orifice [1]. This structure is fundamentally the same whether the jet is generated by a fuel injection system in a scramjet or a reaction control system on the external surfaces of the vehicle.

A vast amount of research (including flight tests) has been conducted on high-speed jet interactions for over 50 years. The bulk of this has concerned the behavior of isolated jets. In his review of jet interaction work in support of supersonic/hypersonic interceptor missiles, Roger [2] includes a bibliography of 169 references (not all publicly available) that cover most of the work performed in North America and Europe on the topic. This includes supersonic low altitude applications (predominantly conventional missiles), fuel injection into supersonic internal flow paths in hypersonic air breathing vehicles, and ultra high-altitude (rarefied flow) hypersonic applications (including NASA's X15 and space shuttle).

Figure 1, from Gruber et al. [3], depicts the basic structure of single porthole jet interactions [4–7]. The key phenomena are: a bow shock caused by the presence of the jet in the supersonic mainstream that interacts with the incoming boundary layer and causes boundary layer separation and recirculating fluid that forms a horseshoe vortex around the jet; a barrel shock terminated by a Mach disk; and a counter-rotating vortex pair. The jet interaction induces high-pressure upstream of the jet, and typically low pressure behind the jet, which can lead to a detrimental pitching moment. Of significance for scramjet fuel systems, the jet penetration into the supersonic mainstream and the subsequent mixing of the injected gas and the air is directly dependent on these flow structures.

In terms of penetration the definition varies between references, however, the most common measurements are based on either injected gas mole fraction or by inspection of Schlieren image intensity. Various studies conclude that the extent of penetration, irrespective of definition, is influenced by several key geometric and flow parameters. These include mainstream Mach number and boundary layer thickness, jet-to-freestream momentum flux ratio, dynamic pressure ratio, degree of jet under-expansion, injector diameter, downstream distance ratio and to a lesser extent injector shape. Molecular weight ratio and Reynolds number effects are much less significant [8–12]. Diamond, circular and square injectors exhibit greater penetration than elongated slot injectors [9], while diamond-shaped injectors provide increased penetration and plume width, reduced total pressure loss and enhanced mixing in comparison with circular injectors [13,14].

The supersonic mixing process of two reacting gases is extremely complex and consists of various transport mechanisms such as species diffusion, heat conduction and momentum exchange between the two fluids [15]. Achieving good penetration across the combustor is of fundamental importance to aid in improved mixing [1] and the degree of mixing is far more dependent on penetration at the injector, than it is on downstream turbulent diffusion [16]. Mixing downstream is also dependent upon on the relative change in jet momentum and for an increased freestream Mach number there is a drastically decreased spreading rate of the supersonic mixing layer, which has a negative effect on the mixing of the injectant [17]. In terms of transverse injection, there are two distinct mixing regions

Presented as Paper 2008-2517 at the 15th AIAA International Space Planes and Hypersonic Systems and Technologies Conference, Dayton, OH, 28 April–1 May 2008; received 6 July 2008; revision received 27 June 2010; accepted for publication 13 July 2010.

*Graduate Student, Center for Hypersonics, School of Mechanical and Mining Engineering. Senior Member AIAA.

†DSTO Chair for Hypersonics, Center for Hypersonics, School of Mechanical and Mining Engineering. Senior Member AIAA.

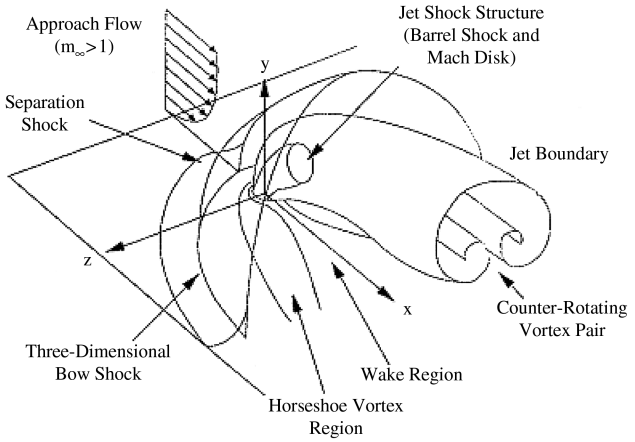

Fig. 1 Basic structure of transverse jet interactions in supersonic flows (from Gruber et al. [3]).

that are governed by different flow mechanisms. The near field region, which is typically 10–20 jet diameters downstream, is driven primarily by the large vortex structures created by the jet-freestream interaction. At downstream distances greater than 20 jet diameters, the far-field mixing is predominantly that of molecular diffusion in the plume/mixing layer [18].

The present work considers the phenomena associated with and the performance of multiple porthole jets, where the jets are positioned close enough to each other that their near field flow structures interact. Both spanwise and streamwise spacing of multiple injectors plays a significant role in penetration and mixing [1]. For example, arrays (3×3) of appropriately spaced and angled fuel injectors in a Mach 2 air stream have been used to form an aerodynamic ramp from the injected fuel [19]. The ramp induced multiple fuel–vortex interactions that had a multiplicative effect, enhancing mixing while reducing total pressure loss, drag and hot spots associated with conventional vortex generators. The jets in the second row also served to increase the pressure behind the first row. Further research investigated the use of multiple fuel–vortex interactions to negate the low pressure region behind single porthole jets [5]: in that work, a single main jet flanked by an array of smaller weaker secondary jets was investigated experimentally and computationally, and the interactions between the jet structures was found to significantly reduce the pitching moment induced by the main jet. Arrays of combinations of diamond-shaped and circular jets (two circular jets flanking a single diamond-shaped jet in a Mach 4 mainstream) have also been studied [20]. In isolation, diamond-shaped jets achieve greater penetration than circular jets. Furthermore, fundamental parametric studies on dual streamwise jets conducted by Lee [21] indicate that multijet mixing, penetration and total pressure recovery performance is closely linked to both streamwise spacing and jet-to-freestream momentum flux ratio, and that an optimum configuration exists.

The beneficial multiplicative effects that have previously been observed for multiple injectors motivate the present study. In this research, simple spanwise arrays of large circular porthole jets are compared with spanwise and streamwise arrays of many (up to 1024 total) small portholes, such that the total fuel mass flux is held constant. The aim has been to determine the relative penetration, mixing and total pressure loss performance between such arrays, and to determine the flow phenomena that give rise to the differences in performance. In particular, the possibility is investigated that upstream jets shield the downstream jets, enabling greater overall penetration than single jets of the same size. Computational fluid dynamics (CFD) has been the tool used to conduct the work. The wall-injection configuration typically used in shock tunnel scramjet tests (four sonic 2 mm-diam holes with equidistant spacing across the scramjet flow path [22]) is systematically modified by simultaneously increasing the number of holes, reducing their diameter and distributing them in both the streamwise and spanwise directions while maintaining fixed total injection cross-sectional area. This is done for sonic injection of hydrogen with global fuel/air equivalence ratio $\phi_{\text{global}} = 0.5$, into supersonic mainstream air with local conditions $P_\infty = 1$ atm, temperature $T_\infty = 1000$ K, Mach number $M_\infty = 4.0$, representative of the combustion chamber of a scramjet flying at approximately $M_\infty = 9.0$. Investigations of the extent to which upstream injectors shield those downstream, with resulting effects on penetration, mixing and total pressure loss, are performed and are reported in this paper.

II. Computational Fluid Dynamics Tool

The commercial code CFD++ [23] was employed in all numerical calculations. The CFD++ code is capable of solving the steady or unsteady Navier–Stokes equations for compressible or incompressible flow, including the modeling of multispecies and finite rate chemistry. The code offers a unified-grid framework allowing the unified treatment of various grid topologies and cell shapes including fully structured, unstructured and hybrid grids. The grid topology independent discretization scheme is total variation diminishing (TVD). Interface fluxes are defined using Riemann solvers based on local wave-model solutions. CFD++ has a wide range of turbulence models that can be integrated directly to the wall or used with advanced wall functions [24]. All calculations in the present study use a steady state implicit (backward Euler) numerical scheme, and three-dimensional second order spatial discretization with TVD polynomial interpolation.

Thermodynamic modeling was performed with curve fits of experimental data [25]. CFD++ offers a range of turbulent Reynolds-averaged Navier–Stokes models. The one-equation Spalart-Allmaras (SA) model was used for the main study with the shear stress transport (SST) model used to determine sensitivity of the results to the choice of turbulence model. To maintain manageable grid sizes a y^+ of approximately five was obtained for all grids using wall functions, and for models requiring integration to the wall a y^+ of less than one was used. In CFD++ the advanced wall functions are capable of reliably working on grids with $0.1 \leq y^+ \leq 300$ while accounting for compressibility, heat transfer and pressure gradient effects. Nevertheless, comparison between the use of wall functions and that of solving the equations to the wall is made here, to assess the sensitivity of the results to the near-wall treatment.

For accurate simulation of the flow present in this problem, the nine-species model proposed by Jachimowski [26] was employed. All calculations reported here were performed with frozen chemistry in order to focus on the penetration and mixing, but enabling the effects of combustion chemistry to be investigated in future investigations by simply switching reactions on and restarting the simulations.

III. Injection Configurations

A. Model Geometry

The geometric model used is the 52 mm-wide, 25 mm-high semi-direct-connect nominally two-dimensional scramjet combustion chamber used by O'Byrne et al. [27] with a typical reference one-jet case consisting of a single spanwise row of four 2 mm-diam injector ports. The computational domain selected for the present study is a small region along the center of the engine in the vicinity of the injector ports, and employs local symmetries in order to reduce computational expense. This area was chosen as it was considered to be relatively undisturbed by the side wall boundary layer interactions, and offered a computational volume of reasonable size given the required grid resolution for the multijet cases. In addition to this, a separate two dimensional CFD calculation was performed on the first 127.5 mm of the full flow domain. This was done in order to produce an inflow profile to the main three-dimensional model that captured the effects of the boundary layer, while further reducing the required three-dimensional grid size and computational time. Figure 2 shows the computational domain within the full flow domain for the reference one-jet case.

This study models four cases representative of the test scramjet engine. The chosen configuration for each case was such that the

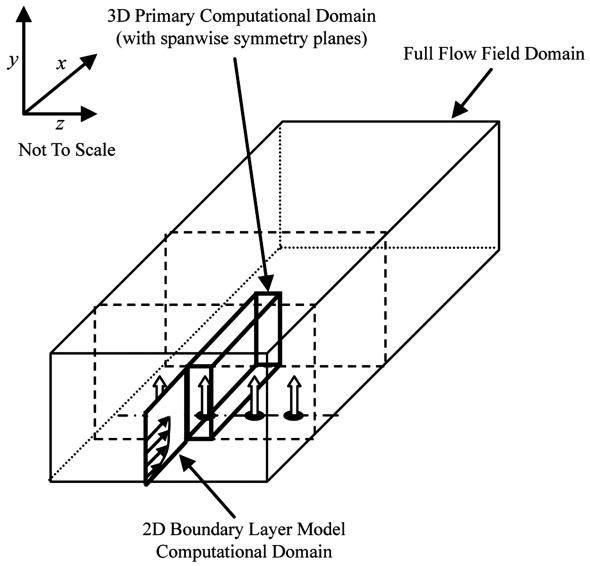

Fig. 2 Scramjet engine geometric arrangement.

injector spacing in both the spanwise and streamwise directions was the same and was equivalent to the reference case, ie. approximately $7d_j$. The injector diameters were 2, 0.5, 0.25, and 0.125 mm, respectively. To maintain a total constant jet area, and therefore maintain the specified equivalence ratio, the required total number of jets was 4, 64, 256 and 1024, respectively. For a given duct width of 52 mm, a spanwise spacing of $7d_j$ dictated a spanwise number of jets of 4, 16, 32, and 64, respectively. This therefore dictated a streamwise number of jets of 1, 4, 8, and 16, respectively.

The dimensions of the primary computational domain were determined from both the derived geometric jet configurations and preliminary coarse grid CFD results for each case. The dimensions were calculated such that the jet plume was sufficiently captured for each case while minimizing unnecessary domain regions. The resulting dimensions are summarized in Table 1 below.

Table 1 shows the number of jets N in the streamwise and spanwise directions in addition to the total number of jets. Also shown are the dimensions of the primary computational domain in the x, **y** and **z** directions, referring to Fig. 2 for the applied coordinate system.

This arrangement implies that the effects of multi port injection will be considered in the context of this engine, and not in isolation. The consequence of this is that the computations for each case will not retain a constant fuel mass flow, but rather the overall scramjet fuel mass flow will remain constant. It was therefore necessary to use an additional parameter that would allow geometric comparison of the multijet to single jet case, taking this into consideration. The parameter of choice is the equivalent jet diameter [1] which is the representative single jet diameter based on the sum of the area of the multijet injectors for a given streamwise row. The required equation is given as

$$d_j^* = \sqrt{\frac{4\Sigma A_j}{\pi}} \tag{1}$$

where ΣA_j is the sum of the areas of each individual jet in the multijet streamwise row. When modeling the injectors for all four cases, it became apparent that the boundary layer effects within the injector pipe itself would become more considerable as the number of jets increased. These effects would produce a non unity discharge coefficient leading to reduced fuel mass flow as the number jets increases. The jet diameter for all cases was therefore modeled based on the assumption that it represents the effective jet diameter such that a constant mass flow is maintained for all cases on the whole. A summary of the geometric parameters in terms of the injectors for each case is shown in Table 2.

Table 2 shows the number of jets in addition to the individual and equivalent jet diameter given by d_j and d_j^* respectively. Finally the area of each jet A_j and that of its respective streamwise row $A_{\text{streamwise}}$ is provided. Each of the four cases models a representative streamwise row of injectors in the center of the scramjet. The streamwise injector spacing has been somewhat arbitrarily selected as $7d_j$, which provides adequate jet separation for all cases. Figure 3 shows scale drawings of the injector region for each of these four cases.

The drawings show that the spanwise width of the computational domain becomes very small as the number of jets is increased, while the overall streamwise length remains relatively constant with the obvious exception of the one-jet case.

B. Computational Grid

Based on the geometric values discussed in the previous section, the resulting four grids were constructed. To facilitate the most rapid grid development given the scale and number of injector ports to be modeled, a hybrid approach was adopted. This approach used an unstructured grid in the x-z plane that was extruded in the y direction to provide a fully structured grid in both the x-y and y-z planes. This was done to ensure accurate capture of the boundary layer region of the flow using the applicable turbulence model. While the adopted method allowed for relatively simple grid construction, the disadvantage was that a stringently consistent grid was not able to be maintained across all four cases. This issue was dealt with by manually attempting to maintain constant cell spacing to injector size ratio. An example of the grid design is shown in Fig. 4 which clearly illustrates the hybrid approach. The sonic wall injectors are modeled as constant diameter pipes beneath the floor of the combustion chamber, to allow the flow from the injectors to not be constrained to move in a specified direction, thus improving convergence of the solution.

IV. Boundary Conditions

The inflow supersonic airstream was chosen to have the local conditions $P_\infty = 1$ atm, temperature $T_\infty = 1000$ K, Mach number $M_\infty = 4.0$. The chosen values are generic but representative of the typical combustor inflow conditions found during shock tunnel experiments. As previously mentioned, a separate two dimensional CFD calculation was performed in order to produce a boundary layer inflow profile for the three-dimensional computational domain. The profile contained essential data on the boundary layer that the

Table 1 Summary of primary computational dimensions

Case	N_{Stream}	N_{Span}	N_{Total}	x_{comp}, m	y_{comp}, m	z_{comp}, m
1	1	4	4	100×10^{-3}	15×10^{-3}	5.20×10^{-3}
2	4	16	64	100×10^{-3}	10×10^{-3}	1.53×10^{-3}
3	8	32	256	100×10^{-3}	10×10^{-3}	787.88×10^{-6}
4	16	64	1024	100×10^{-3}	10×10^{-3}	400.00×10^{-6}

Table 2 Summary of primary computational dimensions

N_{Stream}	N_{Span}	N_{Total}	d_j, m	d_j^*, m	A_j, m^2	A_{Stream}, m^2
1	4	4	2.00×10^{-3}	2.00×10^{-3}	3.1416×10^{-6}	3.1416×10^{-6}
4	16	64	0.50×10^{-3}	1.00×10^{-3}	196.35×10^{-9}	785.398×10^{-9}
8	32	256	0.25×10^{-3}	0.7071×10^{-3}	149.087×10^{-9}	392.699×10^{-9}
16	64	1024	0.125×10^{-3}	0.5×10^{-3}	12.272×10^{-9}	196.350×10^{-9}

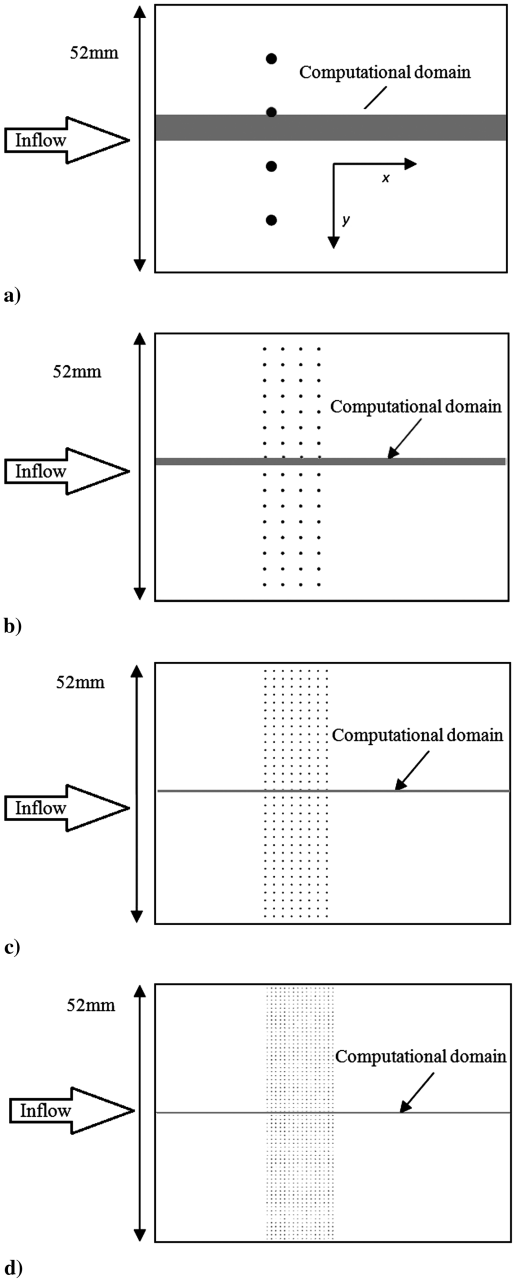

Fig. 3 Case comparison, fuel injection plates: a) 1-jet, b) 4-jet, c) 8-jet, and d) 16-jet.

injectors were to operate within. The purpose of this was to reduce duplicate computations and therefore time, while maintaining a consistent set of inflow conditions to the primary CFD model. The inflow data formed the inflow boundary conditions to the boundary layer inflow profile model.

The sonic fuel inflow boundary conditions were chosen such that the fuel total temperature was 300 K and the pressure was the value required to achieve global fuel/air equivalence ratio $\phi_{\text{global}} = 0.5$.

To take advantage of the natural symmetry of the problem, both the left and right *x-y* planes of the model were given a symmetry boundary condition. This condition provides a mirror image of all scalar and vector quantities in the plane defined by the surface face. The flow velocity becomes tangential to the surface and experiences free slip at the boundary. This tangential velocity is calculated using characteristic relations based on the selected equation set. The lower boundary of the flow domain was set to the viscous (no-slip) wall boundary condition. This condition imposes a zero velocity at the wall, with turbulence quantities being set to their wall-limiting value. The thermal model chosen was an adiabatic—zero heat flux

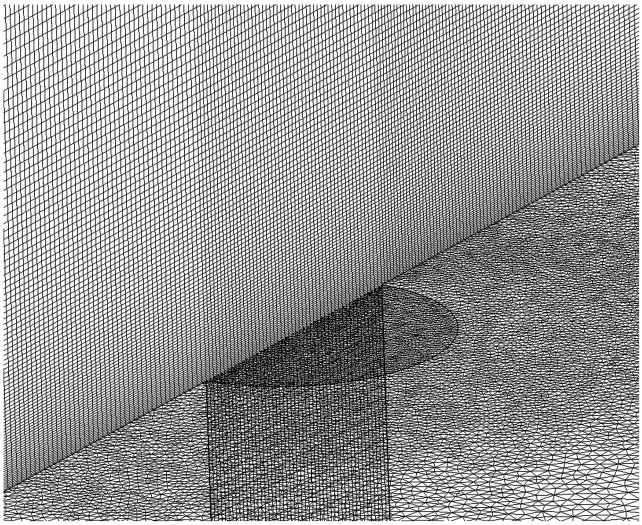

Fig. 4 Computational grid, single-injector case showing cell density in vicinity of the jet.

boundary condition, which when used in conjunction with wall functions accounts for compressibility effects. The walls of the jet inlet pipe were set to an inviscid (slip) wall boundary condition. This selection was based on the fact that resolution of the boundary layer within the injector pipe was not of primary concern in this study. To isolate the results of the pure transverse jet from shock effects, the upper boundary of the computational domain was assigned a supersonic outflow boundary condition rather than a solid wall. This was an acceptable choice since the primary focus of the present study is on the jet in isolation, and therefore the upper wall was not required. In addition to this, the end plane outflow of the domain was also assigned a supersonic outflow.

V. Treatment of Numerical Accuracy

Concerning temporal convergence, all solutions reported here were obtained with an iterative convergence of at least four orders of magnitude in the normalized residuals for each equation solved.

The ordered discretization error of the simulations has been investigated in order to ensure spatial or grid convergence. This is a necessary step to determine whether or not a grid independent result has been achieved. The purpose of the spatial convergence study is to determine the discretization error of the solutions and present it numerically in the form of a grid convergence index (GCI). The calculated GCI will indicate the degree of discretization error for the selected grids as dictated by validation requirements.

To facilitate the spatial convergence study three grids were constructed for the four-jet case, being as labeled fine (1), medium (2) and coarse (3). In the construction of the three grids, a refinement ratio r of approximately two was sought to allow differentiation of the discretization error from other sources such as iterative convergence error. The refinement ratio r refers to the fine/coarse ratio of a selected geometric grid parameter. In the present study, the geometric parameter h was calculated using the global average cell volume. This was chosen since it resulted in reasonable grid sizes when compared with a grid point refinement which would have yielded a fine grid of around 40 million cells. All grid convergence study solutions were obtained with a minimum of four orders of magnitude convergence. While it is recognized that this is not the ideal method of grid refinement, computational resources prohibit a more robust approach to this convergence study. Since one of the primary objectives is to determine mixing, the obvious choice for the key study variable is hydrogen mass fraction. To reduce the possibility of erroneous results, data points were taken along a vertical line at 1 mm intervals, at a distance of 50 mm downstream of the first jet center. This location is beyond the far-field mixing transition point and offers a relatively stable sampling region. The hydrogen mass fraction data along these lines were averaged in order to obtain

Table 3 Grid convergence study data

Grid	Cells	h_n	$\varphi_n = c_{H_2}$
Fine (h_1)	8,942,040	166.769×10^{-15}	0.2253
Medium (h_2)	4,408,650	338.257×10^{-15}	0.2249
Coarse (h_3)	2,272,140	646.465×10^{-15}	0.2234

Table 4 Discretization parameters

Parameter	Value
$r_{21} = h_2/h_1$	2.028
$r_{32} = h_3/h_2$	1.911
$\epsilon_{21} = \varphi_2 - \varphi_1$	−0.0003946
$\epsilon_{32} = \varphi_3 - \varphi_2$	−0.0014820
$p = \frac{1}{\ln(r_{21})}\lvert \ell n \lvert \frac{\epsilon_{32}}{\epsilon_{21}} \rvert + q(p) \rvert$	+2.534
$\varphi_{\text{ext}}^{21} = (r_{21}^p \varphi_1 - \varphi_2)/(r_{21}^p - 1)$	0.22534
$\varphi_{\text{ext}}^{32} = (r_{32}^p \varphi_2 - \varphi_3)/(r_{32}^p - 1)$	0.22523
$e_a^{21} = \lvert(\varphi_1 - \varphi_2)/\varphi_1\rvert$	0.175%
$e_a^{32} = \lvert(\varphi_2 - \varphi_3)/\varphi_2\rvert$	0.659%
$e_{\text{ext}}^{21} = \lvert(\varphi_{\text{ext}}^{21} - \varphi_1)/\varphi_{\text{ext}}^{21}\rvert$	0.00876%
$e_{\text{ext}}^{32} = \lvert(\varphi_{\text{ext}}^{32} - \varphi_2)/\varphi_{\text{ext}}^{32}\rvert$	0.04752%
$\text{GCI}_{\text{fine}}^{21} = (1.25 e_a^{21})/(r_{21}^p - 1)$	0.00876%
$\text{GCI}_{\text{fine}}^{32} = (1.25 e_a^{32})/(r_{32}^p - 1)$	0.04752%

representative single values for each grid. This data was then used for the grid convergence study variable, representing the variable of interest. Grid data relevant to the convergence study can be found in Table 3.

The adopted method is from the Journal of Fluids Engineering Editorial Policy Statement on the Control of Numerical Accuracy and Procedure for Estimation and Reporting of Discretization Error in CFD Applications. The actual GCI calculation was performed numerically, giving the results in Table 4, where p is the apparent order, r is the refinement ratio, e_a is the approximate relative error, e_{ext} is the extrapolated relative error and all other variables represent intermediate calculations. The results in Table 4 indicate that the numerical uncertainty of the averaged hydrogen mass fraction in terms of discretization error is approximately 0.048 and 0.0088% for the medium and fine grids, respectively. Figure 5 shows the change in hydrogen mass fraction with each of the three grid refinements.

Based on these results it is clear that the medium grid exhibits a reasonably low value of discretization error. Therefore all other grids were constructed such that the relative spacing with respect to each grids injector size was maintained as close as possible to the four-jet medium grid. This ensured that the discretization error is subsequently minimized for all grids.

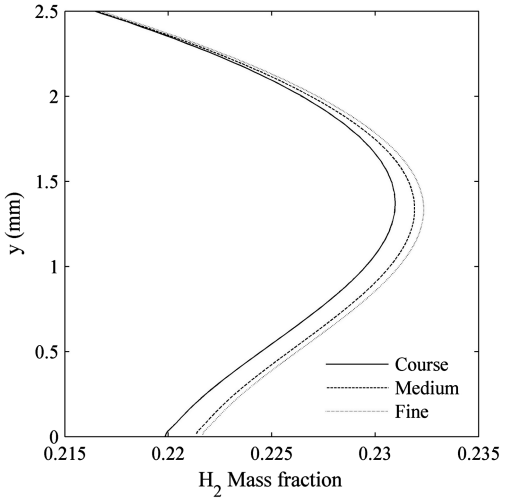

Fig. 5 Hydrogen mass fraction comparison, four-jet case.

An error analysis of the CFD data from the present study has been limited primarily to a quantitative grid convergence study. This was performed to ensure minimal discretization error in the solution data. The results of the grid convergence study suggest this error is very small and is thus considered to be negligible. Further to this, iterative convergence was achieved to a satisfactory level and the associated errors were also considered to be negligible. A detailed sensitivity analysis was not performed in this study, and thus the presence of additional errors is unknown.

VI. Results

A. Validation of Results

When performing a validation of the results of this study through comparison with published work, there were several issues which complicated a direct comparison. The first and foremost of these is the large variation in parameter values chosen among these studies. Differing jet velocities and pressures in addition to boundary layer thicknesses and even the very definition of what constitutes the penetration height were among the issues faced. Also, since the correlations are reported for single port injection only, their use in all but that reference case is not applicable. As a direct consequence of these issues, a comprehensive validation for this study is not performed here. Notwithstanding these problems, a results comparison of some description is required for the purposes of CFD validation, and therefore a limited comparative analysis is presented covering penetration and flow features.

1. Penetration Validation

There is a wide variance in the definition of penetration height among various published literature. To maintain consistency and enable comparison to other published work, a common definition will be adopted as: the penetration is the height above the wall in the y direction where the hydrogen mole fraction of the jet plume reduces to 0.5%. That is the height where $\chi_{H_2} = 0.005$. Unless otherwise specified, all references to penetration in the following chapters are with respect to the jet centerline (symmetry plane).

To validate the results of the present study, the penetration of the single-jet case will be compared with a variety of published results. As previously mentioned, there are many flowfield variables that effect the penetration of a transverse jet, and the model selected must offer an ability to account for these. An example of a typical single-jet correlation is that proposed by Povinelli and Povinelli [28]. This correlation is relevant for single circular injectors and considers jet-to-freestream pressure ratio, jet exit Mach number and jet diameter, where the standard correlation is given as follows:

$$\frac{y}{d_j} = 1.12\left(\frac{p_{0,j}}{p_{\text{eb}}}\right)^{0.483} (M_j)^{0.149}\left(\frac{x_j}{d_j} + 0.5\right)^{0.281} \tag{2}$$

In this correlation $p_{0,j}$ is the total pressure of the jet and p_{eb} is the "effective back pressure," defined as two thirds of the total pressure behind a normal shock in the freestream flow, calculated here as $p_{\text{eb}} = 1.405 \times 10^6$ Pa. M_j is the jet exit Mach number, x is the downstream distance from the first jet center and d_j is the single-jet diameter. To take into consideration the effects of the boundary layer, the momentum thickness θ can be added to Eq. (2) to give a modified version of the Povinelli correlation:

$$\frac{y}{d_j} = 3.21\left(\frac{p_{0,j}}{p_{\text{eb}}}\right)^{0.416} (M_j)^{0.121}\left(\frac{x_j}{d_j} + 0.5\right)^{0.203}\left(\frac{\theta}{d_j}\right)^{0.163} \tag{3}$$

Additional correlations such as those of Rogers [29] and McClinton [30] use the jet-to-freestream dynamic pressure ratio in lieu of Povinelli's effective back pressure definition. Additionally the boundary layer effects are accounted for by the inclusion of a velocity boundary layer thickness term in McClinton's definition. The general form of this correlation is

Table 5 Penetration correlation coefficient values

Study	A	B	C	D
Rogers [29]	3.87	0.3	0.143	0
McClinton [30]	4.2	0.3	0.143	0.057

$$\frac{y}{d_j} = A\left(\frac{q_j}{q_\infty}\right)^B \left(\frac{x_j}{d_j}\right)^C \left(\frac{\delta}{d_j}\right)^E \tag{4}$$

where q_j and q_∞ are the jet and freestream dynamic pressures, respectively, δ is the velocity boundary layer thickness at the jet, the coefficients A, B, C, E and F are dependent upon the particular study, and the remaining variables are equivalent to those described in Eq. (2). In the case of the Rogers and McClinton correlations, the coefficient and index values are given in Table 5 below.

The CFD penetration data has been plotted with the four correlations in Fig. 6. It is clearly evident from Fig. 6 that the standard Povinelli and Rogers correlations show significant deviation from the CFD data of the present study. In contrast to this, both the McClinton and modified version of the Povinelli correlations agree reasonably well with the present prediction of the penetration. This is due to the reduction of momentum in the freestream caused by the presence of the boundary layer that is not considered in the other correlations. This result reinforces the importance of boundary layer effects in transverse injection problems. These results suggest that the single-jet CFD solution is realistic in terms of the downstream penetration.

2. Flow Feature Validation

Comparison of the single-jet CFD results has been made with reference to the flow features presented by Ben-Yakar [31]. There are many factors that will affect the actual structure of the flow such as the Mach number and gas properties of the jet and freestream, in addition to the boundary layer thickness. These factors will cause slight differences in the flow structure between studies; however the primary features will still be present to a degree that will allow qualitative validation. All of the primary features typically found in sonic injection into supersonic crossflow were found to be present. This, in addition to the penetration correlation comparisons above, provides confidence in using the present approach to conduct a parametric investigation of in-line multiport fuel injection.

B. Multijet Flow Structure Analysis

The flowfield of the multijet injection configurations studied here exhibit very different characteristics to what is seen for a typical single jet in a supersonic crossflow. To identify the underlying flow structure several techniques were employed, including inspection of Mach number, pressure, density and hydrogen mass fraction contour plots in addition to stream traces. Based on the investigated CFD results, two distinctly different flowfields were observed in the multijet cases. The four-jet and eight-jet cases exhibit the same characteristics, whereas the 16-jet case shows an alternate behavior.

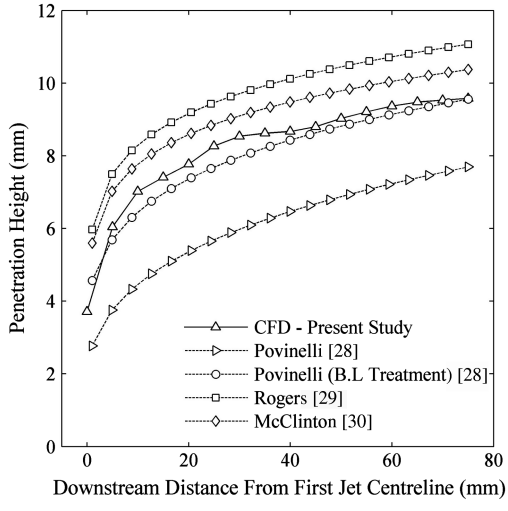

Fig. 6 Single-jet penetration correlations from various studies.

1. Flow Structure (Four-Jet and Eight-Jet Case)

The general flow structure and interaction between two jets located downstream of the second jet in a streamwise row has been constructed and is shown in Fig. 7 below. It should be noted that this model does not show the presence of the upstream injection plumes, and is simply intended to illustrate the interaction between two downstream jets.

In comparison to the single-jet case, the most important contrasting feature illustrated in Fig. 7 is that each of the jets behind the most upstream jet are subjected to a subsonic oncoming flow in the order of approximately $M = 0.3$. While the flow here does not strictly present the same features as expected from a jet in a subsonic crossflow such as that given by Beresh et al. [32], there are similarities. The typical barrel shock and terminating Mach disk is present for all downstream jets as in the subsonic case. There is also no bow shock formed upstream of the jet, due to the subsonic inflow.

Immediately behind each downstream jet is a stagnation point, resulting in reversed flow and the formation of a pair of strong wake vortices adjacent to the rear of the jet. The mechanisms governing the formation of the wake vortices for multijet flow are not the same as for the single-jet case, where the main vortex structures originate from the jet itself. In contrast to this, the multijet wake vortices originate from well behind the jet, being as a result of the interactions between the jet, freestream and reversed flow in that region. These vortices resemble a "twister," and are turned downstream parallel to the wall when encountering the higher velocity of the mainstream flow. The plume exits the jet and is also turned downstream enveloping the two wake vortices.

Since there is no separation or recirculating flow upstream of each jet, the formation of a horseshoe vortex does not occur, although the first jet subjected to the mainstream flow still produces this vortex. In contrast to the single jet, the horseshoe vortex initially wraps around the first jet, then dissipates into the wake vortex behind the second jet. The horseshoe vortex consists primarily of high-temperature air from the boundary layer, which penetrates between the jets until joining the wake vortex. When looking at the combined effect of multiple downstream jets (<8), the result is a "tower" of plume and vortex structures increasing in relative size in the y direction.

2. Flow Structure (16-Jet Case)

As previously mentioned, the 16-jet case is governed by flow phenomena differing from that of the other cases. For jets downstream of the second jet in the streamwise row, the flow has typically the same structure as shown in Fig. 7, however, this is not the case for the first and second jet. The first notable difference is the lack of horseshoe vortex upstream of the first jet. This is replaced by a large separated/recirculation zone that spills over the top of the injection plume and is not drawn into the wake vortices. This recirculating flow carries fuel well forward of the first jet before it joins to the upper region of the main injection plume. These effects are due to the

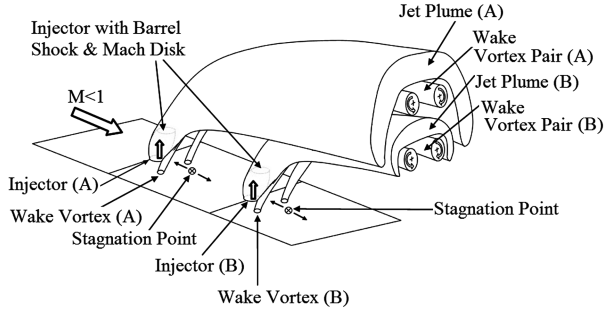

Fig. 7 General flow structure and interaction of multijet injection.

relative spanwise spacing of the 16-jet case: the matrix of jets begins to resemble a two-dimensional ramp of fuel. The lack of three-dimensional relieving effect minimizes penetration of the freestream air into the region between the jets, with the majority of flow passing over the top of the injection plume. An approximately two-dimensional mainstream flow separation results.

The differences in flow structure between the cases have wide implications in terms of the overall performance of the injection configuration. Important aspects such as penetration, mixing, total pressure loss and wall temperature distribution are governed by the underlying physical behavior of the flow in each case. These aspects will be discussed in the following sections.

C. Total Pressure Recovery

An important aspect of any fluid related propulsion system is how well it can perform its intended purpose with a minimum of losses. These losses can manifest themselves in many different ways, and a method of some description is required to quantify them. One of the commonly employed methods investigates the change in total pressure across the system. The relationship between the total pressure and system losses comes about due to entropy production. This quantity offers an indicative measure of the effects of dissipation or flow losses [18]. For the purpose of comparing the production of entropy for each of the injection configurations, and hence the losses, the total pressure will be examined. The definition of mass averaged total pressure adopted is as defined by Lee [21] and given at Eq. (5). This definition will be used only as an indicator of the overall comparative performance of each injection configuration since it does not consider the variation in fuel mass flow for each:

$$P_0(x) = \iint p_o \rho u.\mathrm{d}y.\mathrm{d}z \Big/ \iint \rho u.\mathrm{d}y.\mathrm{d}z \tag{5}$$

The mass weighted total pressure has been normalized by its respective freestream total pressure and plotted in Fig. 8. In the figure, results for two turbulence models (SA and SST) and two different wall treatments [solve to the wall (STW) and wall functions (WF)] are included.

The single-jet reference case exhibits significant total pressure losses whereas improvements for the multijet cases are indicated. In particular, the four-jet case performs significantly better than the single-jet case, and the eight-jet case significantly better than the four-jet case. Asymptotic behavior is observed with respect to the size and number of jets, with the 16-jet case only marginally better than the eight-jet case.

The primary contributions to the results of each configuration is the relative strength of shock and vortex structures. The single jet produces a very strong bow shock in addition to large recirculation zones in the separated region immediately upstream of it. In contrast, the multijet cases tend to produce a much weaker bow shock since they ease into the freestream flow in more gentle ramped-like fashion due to reduced penetration at the front. Figure 9 presents mirror image comparisons of the bow shock strength for each of the multijet cases with respect to a single jet. It is clear that the single jet produces the strongest shock, however, the four-jet case exhibits several distinctly weaker shocks at each of the injection points. The 8-jet and 16-jet cases have no discernible difference in bow shocks, but the 16-jet case has a larger upstream separation zone than the other multijet cases.

In addition to the effects of shocks and separation/recirculation zones, the presence of vortex structures act to increase total pressure loss. As the number of jets is increased, so too does the number of wake vortices in the region behind each injector exit. The losses associated with the formation of these vortices offsets the benefit of reduced bow shock strength as the number of jets is increased.

Concerning the sensitivity of the results to the assumed turbulence model and wall treatment, Fig. 8 indicates that for the single-jet case, there is essentially no difference between the one-equation SA and two-equation SST models using wall functions, and a small increase in total pressure loss when the equations are solved to the wall rather

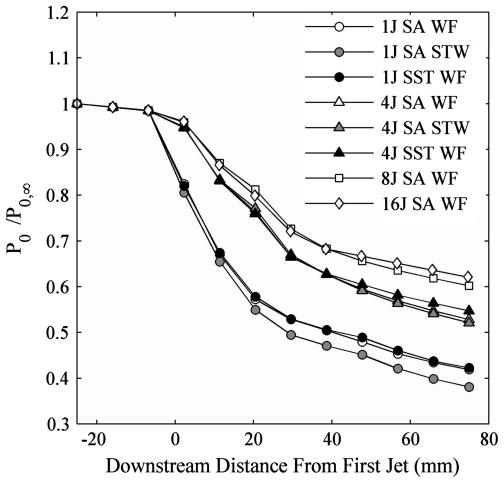

Fig. 8 Total pressure recovery through each injection configuration.

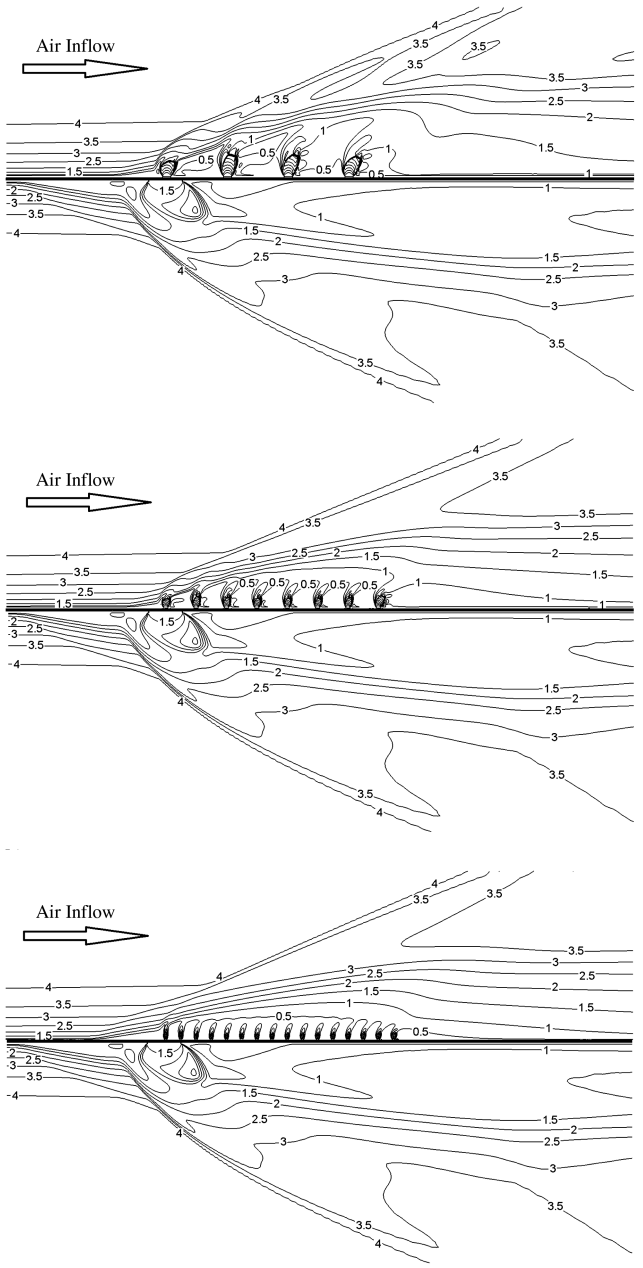

Fig. 9 Comparison of multijet bow shocks (upper half of each plot) to single-jet (lower half) case (Mach number contours).

than employing wall functions. For the four-jet case, there is essentially no difference between the results of the two wall treatments and a small difference between the two turbulence models. In both the single-jet and four-jet cases, these observed differences indicate that the uncertainty in the conclusions of the study with respect to the turbulence model and wall treatment are significantly smaller than the effects on total pressure loss of the number and size of jets employed.

D. Thermal Performance (Wall Temperature)

In terms of the thermal management of a scramjet combustor, material limitations will be a limiting factor in the successful application of an injection system. In addition to this, large temperature gradients can cause thermal stress in the material as a result of the internal stress from local expansion. This can also lead to thermal fatigue over a number of hot-cold cycles, with the same consequences as mechanical fatigue [18]. The thermal aspects of the various injection configurations and their underlying causes are considered here. The computations performed in the present study used an adiabatic wall condition, allowing investigation of temperatures at the wall in the absence of heat transfer and thus representing the worst case scenario. The complex temperature field present in each case required the formulation of a cooling effectiveness parameter as a quantitative measure. The cooling effectiveness parameter developed here is given as

$$C(x) = 1 - \left[\left(\frac{1}{n_z} \sum_{i=1}^{n_z} T_{i,\text{fuel on}} \right)_z \Big/ \left(\frac{1}{n_z} \sum_{i=1}^{n_z} T_{i,\text{fuel off}} \right)_z \right] \quad (6)$$

where $T_{i,\text{fuel on}}$ and $T_{i,\text{fuel off}}$ represent the wall temperature with fuel on and fuel off, respectively. The summation is evaluated over the entire wall surface of each computational domain. The definition presented in Eq. (6) allows overall comparison of the wall temperatures present for each injection configuration accounting for local variations in both the spanwise and streamwise directions. The results are presented in Fig. 10 below.

The 16-jet case clearly exhibits the most significant cooling of all the other cases. As the number of jets is decreased, the cooling benefits of the configuration also decrease. Unlike the total pressure results, however, this parameter is sensitive to the turbulence model and wall treatment.

For example, for the SA model solved to the wall, the four-jet case is more effective than the single-jet case at cooling the wall, whereas for the SA model with wall functions, the single-jet and four-jet cases provide similar cooling effectiveness that is better than that yielded by solving to the wall. Comparing the two turbulence models, with wall functions, there is greater cooling effectiveness with the SA than the SST model for both single-jet and four-jet cases. Furthermore, for SA the single jet is more effective than the four-jet case near the jets, whereas the opposite is true for SST. In summary, for average cooling effectiveness, the streamwise behavior cannot be reliably concluded from these results due to the sensitivity to the turbulence model and wall treatment. Nevertheless, the results do indicate that overall, greater cooling is achieved with more jets.

While the cooling effectiveness plot offers an indicative overall comparison of the thermal characteristics of each case, it does not show the precise location of local temperatures or the presence of large thermal gradients. Investigation of the temperature contours at the wall offers the best method of qualitatively evaluating the performance of each injection configuration in terms of practical considerations. In the following, discussion of the behavior of the flows and their effect on surface cooling is presented for both the near-jet region and the region downstream of the jets. The latter is supported by Fig. 11, which shows spanwise-averaged hydrogen mass fraction wall-normal profiles, 75 mm from the location of the first jet, for the SA turbulence model with wall functions. For the single-jet reference case, cold fuel is carried by the large separated recirculation zone forward of the jet, reducing the wall temperature in that region. In the downstream region, however, large spanwise variations are present with greater temperatures experienced outside the shielded region behind the jet. The higher temperatures around the outside of the single jet correspond to the location of the hotter, well mixed gases in the horseshoe vortex. Improved mixing close to the wall for the single-jet case is indicated by the lower mass fraction of hydrogen resulting in reduced downstream wall cooling.

Investigation of the injection region of the four-jet and eight-jet cases reveals a common wall temperature distribution. Penetration of the hot boundary layer air between the first and second jets displaces the cold hydrogen that would otherwise be present raising the temperature. In addition to this, the smaller separated recirculation zone does not carry sufficient fuel upstream of the first jet to provide adequate cooling in that region. The result of these combined effects is significantly increased local heating in the vicinity of the first two injectors. Downstream of the second jet, however, the wall temperature drops significantly without any large gradients. The improved downstream cooling of the eight-jet case is evident, resulting from poor mixing at the wall indicated by the greater fraction of hydrogen present.

This is again seen in the 16-jet case where the most significant improvement in cooling performance is seen. Since the hot boundary layer air does not penetrate between the jets, and the separated recirculation zone extends well forward of the first jet, there is no localized heating in the injection region. In addition to this the downstream wall experiences significantly improved cooling with no spanwise temperature gradients evident. This improvement can be attributed to both the initial cooling upstream, and the film cooling

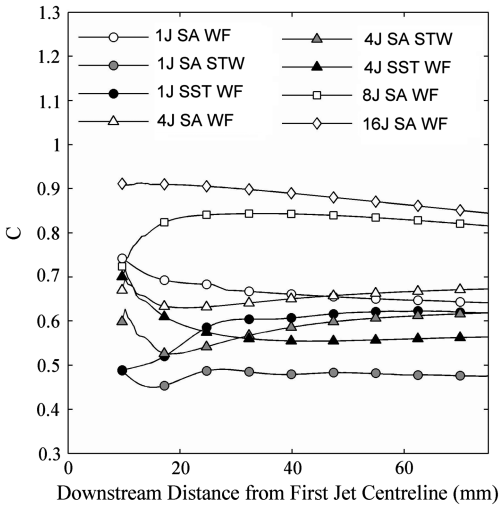

Fig. 10 Cooling effectiveness for each injection configuration.

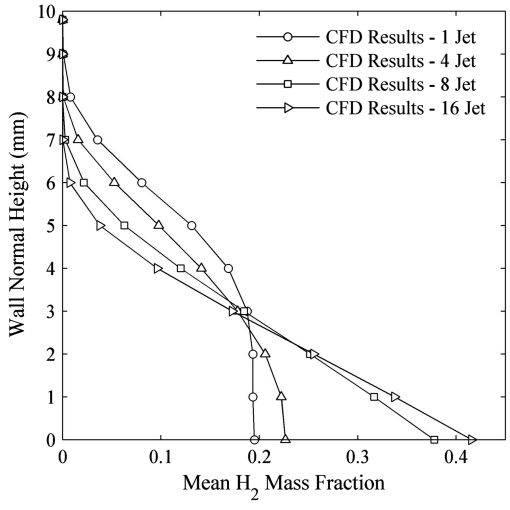

Fig. 11 Spanwise-averaged hydrogen mass fraction distribution ($x_j = 75$ mm).

effect of having a greater mass fraction of cold unmixed hydrogen available at the wall.

In terms of thermal issues, the four-jet and eight-jet cases present the greatest challenge. The high temperatures near the injectors have the potential to erode the fine edges of the injector port lip in addition to causing changes in port shape and size due to local material expansion. It is believed that the presence of cold fuel passing through passages in the wall material in this region would improve local cooling. There is also potential for the hot regions in the four-jet and eight-jet cases to facilitate ignition given the appropriate conditions. Further study is required to validate these assumptions.

E. Penetration

Penetration data was obtained at 16 streamwise stations of 5 mm spacing by measuring the penetration height along the jet centerline in accordance with the mole fraction definition described earlier. Data was analyzed for all cases and is presented in Fig. 12 showing the streamwise penetration. Also included is the modified Povinelli single-jet correlation previously presented in Eq. (3).

It is clear from these results that the absolute penetration is reduced for the multijet cases. This is due to the reduction in equivalent jet diameter as the number of jets is increased. However, as will be discussed further below, the penetration for multiple jets is almost as much as for the single jet, despite their much smaller jet diameters. In the near field ($x \leq 20$ mm) the single jet exhibits a substantially different penetration behavior when compared with the multijet cases. For the single-jet case, the near field penetration is initially well beyond the boundary layer, with a curved steep penetration trajectory. In contrast, the multijet cases do not initially penetrate beyond the boundary layer, but then exhibit an almost linear penetration in the near field. It is also worth noting that the multijet cases demonstrate near identical penetration in the near field region, suggesting a possible limiting value.

When the penetration is nondimensionalized against the equivalent jet diameter [Eq. (1)], additional aspects of the behavior are observed as shown in Fig. 13.

The dimensional penetration results indicate a sensitivity to turbulence model choice and wall treatment, with the uncertainty band reducing for the four-jet case when compared with the single jet. This variation is far less obvious when the penetration is nondimensionalized. The nondimensionalized penetration allows the effects of number of jets to be isolated from the modelling choices, with the trends clearly evident. The nondimensionalized penetration parameter offers a comparison taking into account the reduced mass flow of the multijet cases. A substantial increase in "equivalent" penetration can be gained by increasing the number of jets in the streamwise direction. The relative magnitude of the penetration parameter results in Fig. 13 suggests the presence of an additional

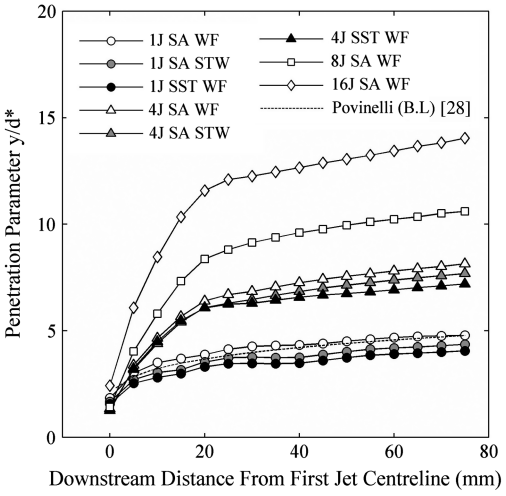

Fig. 13 Nondimensional jet penetration.

factor that enhances the degree of penetration for multiple jets when compared with the same mass flow through a single jet. These gains in penetration occur primarily in the near field region, with the rate of relative penetration change between cases becoming constant in the transition to far field ($x \geq 20$ mm).

The near field boost in the multijet penetration is caused by a similar mechanism to the boundary layer effects discussed previously. Jets are subjected to an increased jet-to-freestream momentum flux ratio when located behind an upstream jet as described by Lee [21]. The presence of a stagnation point and reversed flow in the region between each jet aids in the reduction of freestream momentum, thus improving relative penetration. The upstream jets are essentially shielding the downstream jets, and we term this multijet behavior the shielding effect. This provides an explanation for the differing penetration trajectories between the single-jet and multijet cases: the large single jet penetrates quickly but is rapidly deflected and follows the observed curved path in the near field. On the other hand, in the multijet cases the downstream jets are shielded, can penetrate further than the upstream jets would in isolation, and in turn the upstream jets are supported from beneath by the downstream jets and are not deflected as much by the oncoming flow as they would be in isolation. The overall near field penetration trajectory is thus approximately linear, since the jets are distributed in a linear streamwise arrangement. The general trend is not dependent on the choice of turbulence model or wall treatment.

This effect is further demonstrated by Fig. 14, which shows the actual CFD penetration results along the jet centerline at the outflow boundary ($x_j = 75$ mm) compared with the penetration predicted by

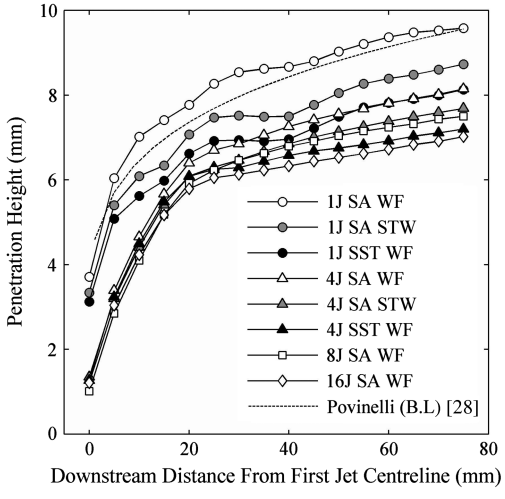

Fig. 12 Dimensional jet penetration.

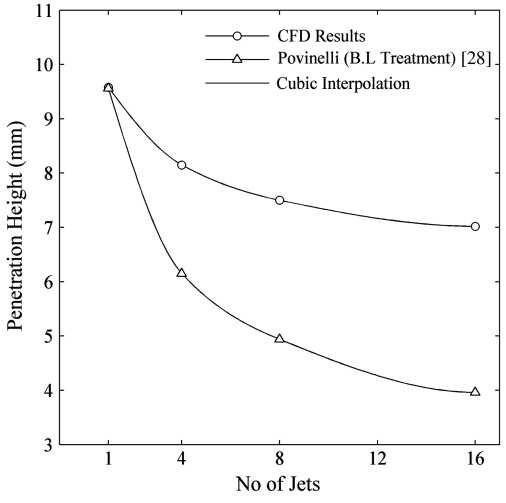

Fig. 14 Multijet penetration at $x_j = 75$ mm.

the modified Povinelli correlation for a single jet with the same equivalent diameter d_j^*.

It is obvious that the CFD far-field penetration is significantly improved when compared with the predicted penetration for the same mass flow through a single injector. As previously mentioned, the results of Fig. 13 indicate a trend in the far field suggesting the relative changes in penetration between the cases are negligible at distances greater than 20 mm downstream. It is therefore assumed that the results in Fig. 14 above will retain their general shape, with the entire plot shifting upward as the penetration increases with increased downstream distance. Further experimental or CFD data would be required to validate this assumption.

F. Development of a Multijet Penetration Correlation

The penetration validation study performed earlier shows that the modified Povinelli correlation provides a reasonable prediction of the single-jet penetration. In the development of a multijet correlation, the modified Povinelli correlation will again be used with the addition of a multijet correction factor. For the purposes of the present study, the Povinelli coefficients will be recalculated in order to obtain a more accurate fit to the single-jet CFD data. In this case, however, given the two distinct penetration behaviors in the near and far field, the following data fits will only account for the far-field data, and thus near field data will be ignored. The general Povinelli penetration equation is given by

$$\frac{y}{d^*} = a\left(\frac{p_{0,j}}{p_{\text{eb}}}\right)^b (M_j)^c \left(\frac{x}{d^*} + 0.5\right)^e \left(\frac{\theta}{d^*}\right)^f \tag{7}$$

where the variables have the same meaning as described earlier, and the coefficients a, b, c, e and f are to be determined. The coefficients to Eq. (7) were obtained through numerical curve fits, and are presented in Table 6 below:

The resulting curve fit is obtained with an R-square value of 0.976, indicating that 97.6% of the variance in the data is explained by the fit. The resulting equation, applicable to the far-field region, will be referred to as the adjusted Povinelli correlation, and is given by

$$\left(\frac{y}{d^*}\right)_{\text{adj}} = C_{mj}(1.896)\left(\frac{p_{0,j}}{p_{\text{eb}}}\right)^{0.9665} (M_j)^{0.3817} \times \left(\frac{x}{d^*} + 0.5\right)^{0.1535} \left(\frac{\theta}{d^*}\right)^{0.01568} \tag{8}$$

where C_{mj} is the multijet correction factor to be determined. Adjusted Povinelli correlation fits based on Eq. (8) above, with appropriate equivalent jet diameter and momentum thickness included, give values of C_{mj} presented in Table 7 below:

To obtain a multijet correction factor for an arbitrary number of jets in the range $1 \le N_j \le 16$, a curve fit to the data in Table 7 must be calculated. A 2 term power fit with resulting R-square = 0.998 was determined from the correction coefficients to give the multijet correction function as follows:

Table 6 Adjusted Povinelli correlation coefficients

Case	a	b	c	e	f	R-square
One-jet	1.896	0.9665	0.3817	0.1535	0.01568	0.976

Table 7 Multijet correlation factors

Case	C_{mj}	R-square
1-jet	1.000	N/A
4-jet	1.483	0.973
8-jet	1.840	0.982
16-jet	2.304	0.978

$$C_{mj} = 0.5N_j^{0.322} + 0.5 \tag{9}$$

In the above equation the number of jets is represented by $N_j = 1, 2, 3 \ldots 16$. Application of this correction function requires appropriate adjustment of the other variables in the correlation at Eq. (8), with specific notice given to the changing nondimensional momentum thickness. Application of the multijet correction function to the far-field CFD data is shown in Fig. 15 below:

It is clear that the correction function yields reasonable prediction of the penetration of varying number of jets. This function is applicable to the specific geometric and flow conditions of the present study up to a downstream distance of 75 mm, and therefore may not provide accurate prediction of penetration with variation in other parameters such as pressure ratio and jet exit Mach number or at greater downstream distances. Further data of a more generic nature including a parametric study would be required in order to produce a more widely applicable correction function.

G. Mixing

A quantitative measure of mixing efficiency is required to assess the relative performance of each injection configuration. The adopted definition of mixing efficiency for this study has been adapted from Lee [21] and is presented as follows:

$$\eta_{\text{mix}}(x) = \iint c^r_{H_2} \rho u.\text{dy}.\text{dz} \Big/ \iint c_{H_2} \rho u.\text{dy}.\text{dz} \tag{10}$$

where

$$c^r_{H_2} = \begin{cases} c_{H_2} & c_{H_2} \le c^{\text{stoic}}_{H_2} \\ \left(\frac{1-c_{H_2}}{1-c^{\text{stoic}}_{H_2}}\right) c^{\text{stoic}}_{H_2} & c_{H_2} > c^{\text{stoic}}_{H_2} \end{cases} \tag{11}$$

with $c^{\text{stoic}}_{H_2}$ defined as the stoichiometric hydrogen mass fraction for a fuel/air mixture. To calculate the mixing efficiency defined in Eq. (10) fifteen slices were taken in the y-z plane at 5 mm intervals in the streamwise direction, commencing at 5 mm downstream of the first jet. The results are plotted in Fig. 16.

In terms of the turbulence modeling, the single-jet case presents a significant spread in the calculated mixing efficiency, and in particular where a different turbulence model has been selected. The four-jet case was less effected by turbulence modeling choices although variations exist. The results for the 8-jet and 16-jet cases lie within the uncertainty band of the single-jet case due to modelling choices, and therefore no conclusive observations can be made. The results do, however, indicate reasonably large improvements in mixing efficiency for the four-jet case when compared with all other cases. All of the cases indicate linear mixing trends in the far field

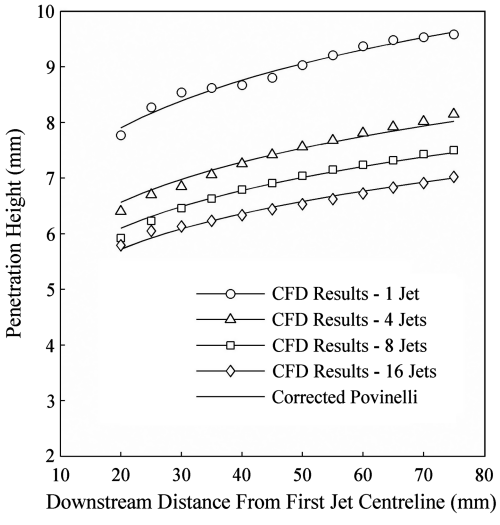

Fig. 15 Multijet correction function data fits.

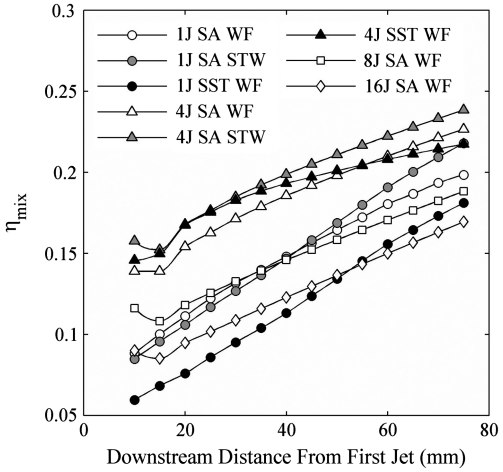

Fig. 16 Multijet streamwise mixing efficiency.

($x > 20$ mm), with slight variations in the mixing rate. An overall increase of approximately 5% in the mean mixing efficiency was observed for the four-jet case when compared with the standard single jet, which resulted primarily from enhanced mixing in the near field.

The near field mixing improvement results from the combined effect of several flow phenomena that occur in the region between the jets. The first and foremost of these is the presence of strong wake vortices between each jet which provides an additional intermediate stirring action. There is a reduction in wake vortex strength in the 16-jet case compared with the other multijet configurations due to a reduction of the insurgence of air between the injectors as a result of decreased spanwise spacing. These factors combined with the absence of horseshoe vortices contribute to the degraded mixing efficiency of the 16-jet case compared with the other multijet cases. In the four-jet and eight-jet cases, there is an increase in mixant interface area due to entrainment of air in the wake vortex region between each of the injectors. These combined effects act to enhance the near field mixing, thus improving overall mixing efficiency when compared with the single-jet case. This suggests that the boost in mixing efficiency is primarily in the near field region, and the diffusion processes downstream are independent of the near field mixing as suggested by Heiser and Pratt [18].

VII. Conclusions

The purpose of this study was to investigate the effect of using a large number of small holes for injection of hydrogen into a scramjet combustor as opposed to a typical single jet. The specific goals included determination of both the penetration and mixing of each of these configurations under a specified set of flow conditions, and quantifying any relationships between these flow aspects and the different configurations. Further to this, identification of the underlying flow mechanisms was performed. The results presented in the investigation have allowed a deeper understanding of the effects of multijet injection in the context of scramjet combustors.

From the literature, a benchmark by which validation of the single-jet reference case validation could be performed was obtained. While the published work relating to multijet injection in the context of scramjet combustors is very limited, the single-jet data offered a starting point by which the present work was based.

The multijet results were analyzed from a number of aspects. First, a validation of the single-jet reference case was performed in order to assess the ability of the CFD code to accurately reproduce the complex flows encountered by transverse injection into a supersonic crossflow. This validation was carried out in terms of the injectant penetration and the presented flow structures. This analysis showed good agreement between the CFD results of the single-jet reference case and published data, improving confidence in the multijet solutions which remain to be validated.

The flow structures in the multijet cases were investigated, which presented a differing flow structure than that of a single jet. It is important to note that the fine details of the flows studied are sensitive to the choice of turbulence model and wall treatment but the observed trends and conclusions are not. A distinct change in the flow structure occurred somewhere between the 8-jet and 16-jet case, where the flow took on a more two-dimensional behavior due to the lack of relieving effect as the spanwise spacing reduced. A flow model for intermediate injectors of a multijet array was constructed, showing the differences compared with the single jet. Improvements in total pressure recovery were also found as a result of the weaker bow shocks present in the multijet cases. These improvements increased but asymptoted as the number of jets increased. For the intermediate multijet cases, reduced cooling performance in the injector region was observed. This led to high temperatures near the first two jets in the streamwise row caused by the insurgence of hot boundary layer air between the injectors. It is assumed that the magnitude of this effect may be reduced by the passage of cold fuel through the injector ports, requiring additional data to confirm.

It was found that for the geometric arrangement studied, the injectant penetration reduced as the jet diameter was reduced and the number of injectors was increased, but penetration was significantly better than for single jets of the same equivalent diameter. When the penetration was nondimensionalized against the equivalent jet diameter, a very significant improvement in near field penetration was observed. This was attributed to a shielding effect resulting from the increase in jet-to-freestream momentum ratio for each downstream injector. Based on the CFD data, a penetration correction function was formulated for use with an adjusted Povinelli correlation. This resulted in reasonable prediction of far-field penetration for multiple jets under the conditions of the present study. Further data is required to enable formulation of a more robust and widely applicable multijet penetration correlation.

Finally, the mixing of the multijet cases was investigated and compared with the single-jet reference case. Significant improvements in near field mixing were observed for the four-jet case with overall improvements of around 5% over a single jet indicated by the mean mixing efficiency. This was attributed to the presence of intermediate stirring due to wake vortices behind each jet, and increased mixant interface area resulting from entrainment of air between jets. No improvements were realized by the 8-jet and 16-jet cases suggesting that there are an optimum number of jets required to maximize mixing performance, although further data is required to assess this. Overall, however, the results presented here, while applicable to the narrow set of conditions prescribed at the outset of the project, offer insight into the potential gains in performance of injection through a large number of small jets when compared with a single jet.

Acknowledgment

The high-performance computing infrastructure support of Australia's National Computational Infrastructure National Facility is gratefully acknowledged.

References

[1] Kutschenreuter, P., "Supersonic Flow Combustors," *SCRAMJET Propulsion*, edited by E. T. Curran, and S. N. B. Murthy, AIAA, Reston, VA, 2000.

[2] Roger, R. P., "The Aerodynamics of Jet Thruster Control for Supersonic/Hypersonic Endo-Interceptors: Lessons Learned," AIAA Paper 99-0804, 1999.

[3] Gruber, M. R., Nejad, A. S., Chen, T. H., and Dutton, J. C., "Bow Shock/Jet Interaction in Compressible Transverse Injection Flowfields," *AIAA Journal*, Vol. 34, No. 10, 1996, pp. 2191–2193. doi:10.2514/3.13372

[4] Champigny, P., and Lacau, R. G., "Lateral Jet Control for Tactical Missiles," Special Course on Missile Aerodynamics, AGARD R-804, Paper No. 3, 1994.

[5] Viti, V., Wallis, S., Schetz, J. A., Neel, R., and Bowersox, R. D. W., "Jet Interaction with a Primary Jet and an Array of Smaller Jets," *AIAA Journal*, Vol. 42, No. 7, 2004, pp. 1358–1368.

[6] Sriram, A. T., and Mathew, J., "Improved Prediction of Plane Transverse Jets in Supersonic Crossflows," *AIAA Journal*, Vol. 44, No. 2, 2006, pp. 405–408.
[7] Manna, P., and Chakraborty, D., "Numerical Investigation of Transverse Sonic Injection in a Non-Reacting Supersonic Combustor," *Proceedings of the Institution of Mechanical Engineers. Part G, Journal of Aerospace Engineering*, Vol. 219, No. 3, 2005, pp. 205–215.
[8] Billig, F. S., Orth, R. C., and Schetz, J. A., "The Interaction and Penetration of Gaseous Jets in Supersonic Flow," NASA CR-1386, July 1969.
[9] Foster, L. E., and Engblom, W. A., "Computation of Transverse Injection into Supersonic Crossflow with Various Injector Orifice Geometries," 42nd AIAA Aerospace Sciences Meeting and Exhibit, Reno, NV, Jan. 2004.
[10] Dowdy, M. W., and Newton, J. F., Jr., "Investigation of Liquid and Gaseous Secondary Injection Phenomena on a Flat Plate with M Equals 2.01 to M Equals 4.54," NASA CR-53063, Dec. 1963.
[11] Billig, F. S., Cameron, J. M., and Wagner, J. P., "Penetration and Spreading of Transverse Jets of Hydrogen in a Mach 2.72 Airstream," NASA CR-1794, March 1971.
[12] Portz, R., and Segal, C., "Penetration of Gaseous Jets in Supersonic Flows," *AIAA Journal*, Vol. 44, No. 10, 2006, pp. 2426–2429. doi:10.2514/1.23541
[13] Grossman, P., Maddalena, L., and Schetz, J., "Flush-Wall, Diamond-Shaped Fuel Injector for High Mach Number Scramjets," *Journal of Propulsion and Power*, Vol. 24, No. 2, 2008, pp. 259–266. doi:10.2514/1.29956
[14] Srinivasan, R., and Bowersox, R., "Transverse Injection Through Diamond and Circular Ports into a Mach 5.0 Freestream," *AIAA Journal*, Vol. 46, No. 8, 2008, pp. 1944–1962. doi:10.2514/1.29253
[15] Ferri, A., Moretti, G., and Slutsky, S., "Mixing Processes in Supersonic Combustion," NASA CR-57127, 1964.
[16] Morganthaler, J. H., "Supersonic Mixing of Hydrogen and Air. Silver Spring," NASA CR-747, April 1967.
[17] Ali, M., Sadrul Islam, A. K. M., and Ahmed, S., "Mixing and Flame Holding with Air Inlet Configuration in Scramjet Combustor," *International Communications in Heat and Mass Transfer*, Vol. 31, No. 8, 2004, pp. 1187–1198. doi:10.1016/j.icheatmasstransfer.2004.08.016
[18] Heiser, W. H., and Pratt, D. T., "Hypersonic Airbreathing Propulsion," AIAA Education Series, AIAA, New York, 1994.
[19] Fuller, R. P., Wu, P. K., Nejad, A. S., and Schetz, J., "Comparison of Physical and Aerodynamic Ramps as Fuel Injectors in Supersonic Flow," *Journal of Propulsion and Power*, Vol. 14, No. 2, 1998, pp. 135–145. doi:10.2514/2.5278
[20] Schetz, J., Maddalena, L., Throckmorton, R., and Neel, R., "Complex Wall Injector Array for High-Speed Combustors," *Journal of Propulsion and Power*, Vol. 24, No. 4, 2008, pp. 673–680. doi:10.2514/1.36660
[21] Lee, S., "Characteristics of Dual Transverse Injection in Scramjet Combustor, Part 1: Mixing," *Journal of Propulsion and Power*, Vol. 22, No. 5, 2006, pp. 1012–1019. doi:10.2514/1.14180
[22] Paull, A., and Stalker, R. J., "Scramjet Testing in the T3 and T4 Hypersonic Impulse Facilities," *SCRAMJET Propulsion*, edited by E. T. Curran, and S. N. B. Murthy, AIAA, Reston, VA, 2000.
[23] Goldberg, U., Peroovian, O., Chakravarthy, S., and Sekar, B., "Validation of CFD++ Code Capability for Supersonic Combustor Flowfields," AIAA Paper 97-3271, 1997.
[24] Metacomp Technologies, "CFD++ User Manual: Ver. 2.6.5," Metacomp Technologies, Agoura Hills, CA, 2006.
[25] McBride, B. J., Heimel, S., Ehlers, J. G., and Gordon, S., "Thermodynamic Properties to 6000 K for 210 Substances Involving the First 18 Elements," NASA SP-3001, 1963.
[26] Jachimowski, C. J., "An Analytical Study of the Hydrogen–Air Reaction Mechanism with Application to Scramjet Combustion," NASA Langley Research Center, Rept. NASA TP-2791, 1988.
[27] O'Byrne, S., Stotz, I., Neely, A. J., Boyce, R. R., Mudford, N. R., and Houwing, A. F. P., "OH PLIF Imaging of Supersonic Combustion Using Cavity Injection," AIAA/CIRA 13th International Space Planes and Hypersonics Systems and Technologies, Capua, Italy, 2005.
[28] Povinelli, F. P., and Povinelli, L., "Correlation of Secondary Sonic and Supersonic Gaseous Jet Penetration into Supersonic Crossflows," NASA Lewis Research Center, Rept. NASA TN-D-6370, 1971.
[29] Rogers, R. C., "A Study of the Mixing of Hydrogen Injected Normal to a Supersonic Airstream," NASA Langley Research Center, Rept. NASA TN-D-6114, 1971.
[30] McClinton, C., in Petit, B., and Robert, A. M., "Ramjets and Scramjets," *Encyclopedia of Physical Science and Technology*, Academic Press, New York, 2001.
[31] Ben-Yakar, A., "Experimental Investigation of Mixing and Ignition of Transverse Jets in Supersonic Crossflows," Ph.D. Dissertation, Stanford Univ., Dept. of Mechanical Engineering, Stanford, CA, 2000.
[32] Beresh, S. J., Henfling, J. F., Erven, R. J., and Spillers, R. W., "Penetration of a Transverse Supersonic Jet into a Compressible Subsonic Crossflow," *AIAA Journal*, Vol. 43, No. 2, 2005, pp. 379–389.

J. Oefelein
Associate Editor